

## TOPICAL REVIEW

# Strain induced semiconductor nanotubes: from formation process to device applications

**Xiuling Li**

Department of Electrical and Computer Engineering, Beckman Institute of Advanced Science and Technology, University of Illinois, 208 N Wright Street, Urbana, IL 61801, USA

E-mail: [xiuling@illinois.edu](mailto:xiuling@illinois.edu)

Received 15 April 2008, in final form 23 July 2008

Published 15 September 2008

Online at [stacks.iop.org/JPhysD/41/193001](http://stacks.iop.org/JPhysD/41/193001)**Abstract**

Semiconductor nanotubes (SNTs) represent a new class of nanotechnology building blocks. They are formed by a combination of bottom-up and top-down approaches, using strain induced self-rolling mechanism from epitaxially grown heterojunction films. This review summarizes several aspects of this emerging field, including the SNT formation process, its dependence on crystal orientation, strain direction and geometry as well as the structural, electronic and optical properties and their implications. The precise controllability of structural and spatial positioning and versatile functionality make SNTs and related three-dimensional (3D) architectures promising candidates for practical applications in next generation nanoelectronic and nanophotonic devices.

(Some figures in this article are in colour only in the electronic version)

**1. Introduction to semiconductor nanotubes (SNTs)**

The most widely studied type of nanotube is perhaps the carbon nanotube (CNT), first introduced by Iijima *et al* in 1991 [1]. A simple search of 'CNT' in the Engineering Village database yields more than 49 000 citations. CNTs can be formed by methods such as chemical vapour deposition [2–5], vapour liquid solid growth [6], arc discharge [1] and laser ablation [7]. Their perfect molecular structure attracted considerable basic research interest and their distinct physical, electronic and mechanical properties have led to extensive research efforts to explore their applications in many fields including nanoelectronic devices for memory storage, interconnects and biomedical sensing [8–13]. Another type of interesting nanotube is the highly ordered TiO<sub>2</sub> nanotube arrays made by anodic oxidation of titanium. The material architecture has proven to be of great interest for use in water photoelectrolysis, photocatalysis, heterojunction solar cells, and gas sensing [14].

The SNT, a new paradigm, is formed by an entirely different process, a combination of bottom-up and top-down approaches. SNTs were first fabricated by Prinz *et al*

from Russia in 2000, using strain induced self-rolling of In<sub>x</sub>Ga<sub>1-x</sub>As/GaAs semiconductor bilayers grown by molecular beam epitaxy (MBE) [5]. The same group introduced Ge<sub>x</sub>Si<sub>1-x</sub>/Si self-rolled nanotubes [16]. The basic concept of the rolling mechanism of SNTs is illustrated in figure 1. For a layer with lattice constant larger than the substrate, e.g. the InAs layer on an InP substrate in figure 1(a), it is compressively strained when pseudomorphically deposited on the substrate (figure 1(b)); while the GaAs layer is tensile strained. When the sacrificial layer (e.g. AlAs in figure 1) is selectively etched away, the strained bilayer that consists of GaAs and InAs becomes detached from the substrate (figure 1(c)). The compressively strained InAs layer deforms to expand with force  $F_1$ , while the GaAs layer on top resists the expansion with force  $F_2$ . This results in a momentum  $M$  which drives the rolling action to form a tube (figure 1(d)) in order to accommodate the relative strain within the InAs/GaAs bilayer. Depending on the undercut extent, single or multi-wall tubes can be formed. SNTs formed this way have also been named RUNTs for rolled up nanotubes [17].

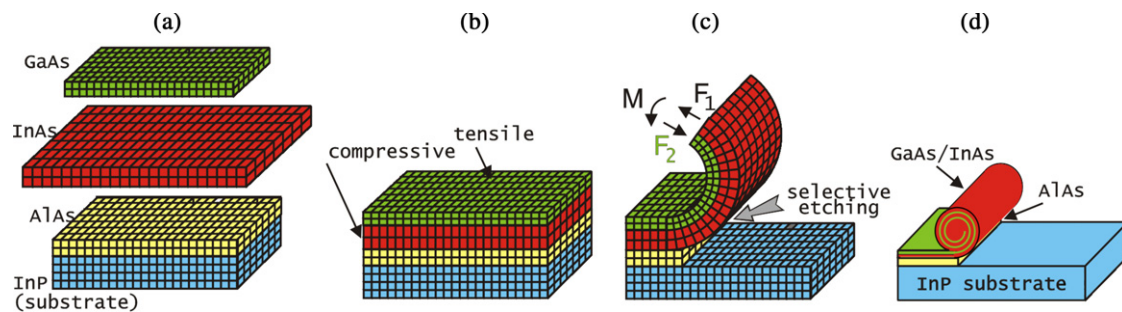


**Figure 1.** The formation mechanism of strain induced self-rolling III–V SNTs, illustrated with a InAs/GaAs bilayer and a AlAs sacrificial layer. Reprinted from [18] copyright 2003 with permission from Elsevier.

There are two essential components in strain induced self-rolling structures: (1) a sacrificial layer that can be selectively etched off from the layers above it and the substrate; (2) a bilayer above the sacrificial layer consisting of two different materials that are relatively strained from each other or a single material with regions of different strains [19]. The strained bilayer is the moving part that is powered by strain release. The formation approach involves epitaxial growth (bottom–up) which determines the composition and thickness (thus diameter) of the rolling component, and lithographic processing (top–down) which controls the length, position and shape of the final nanostructure. This concept should apply to all epitaxial material systems as long as the two essential components are present, including Si–Ge, III–V, II–VI semiconductors, as well as composite materials that involve metals [20] and polymers [21], etc. Nanotubes with inner diameters as small as 3 nm were formed from ultra-thin InAs/GaAs films [15, 22]. For hybrid nanotubes, self-assembled monolayers (SAMs) have been deposited on a  $\text{In}_x\text{Ga}_{1-x}\text{As}/\text{GaAs}$  bilayer to form radial superlattices [23]; tubular structures of SiGe/SiO<sub>x</sub>/Ti [24] and  $\text{In}_{0.3}\text{Ga}_{0.7}\text{As}/\text{Cr}$  [25] have been reported; and SiGe/Si/SiN/Cr nanoshells have been demonstrated [26, 27]. The strain induced formation mechanism has also been generalized to form various other kinds of 3D architectures [28–30]. In addition, the rolled up tubes can be embedded by epitaxially overgrown films to form hollow micro- or nanochannels in semiconductor materials [15, 18].

Potential applications have been envisioned [31] and some preliminary results have been demonstrated. For example, SNTs can serve as micro- or nanoscale building blocks for MEMS and NEMS, micro-injections and ink-jet printing [32], etch mask for nanofabrication [33], magnetic conductors using ferromagnetic material filled coils [34], x-ray waveguiding [35], fluidics [24, 36, 37] and biology [38]. The broad spectrum of possible applications of SNTs has attracted both theorists and experimentalists around the world. However, major involvement is still very limited.

This review intends to summarize published pioneering work in the field of strain induced self-rolled semiconductor 3D architectures, as well as recent results from author's own research group, with a focus on SNTs. It is organized to include the following sections: the formation process, structural, electronic, optical properties and device prospects, and concluding remarks.

## 2. SNT formation

### 2.1. Growth and fabrication methods

In order to form a SNT using the strain-driven mechanism, the first step is the planar epitaxial growth of the strained bilayer structure with the sacrificial layer underneath. Both MBE and metalorganic chemical vapour deposition (MOCVD) were used for deposition. The next step is to expose the sacrificial layer to the etchant so that the bilayer can be released from the substrate. This can be done by simply making a scratch on the wafer [34, 39], selectively growing on the sidewall [40], or by a more controllable, systematic and manufacturable way such as lithographical patterning [25, 26, 29, 41–43]. For arsenide based structures, high composition  $\text{Al}_x\text{Ga}_{1-x}\text{As}$  is commonly used as sacrificial layers. In addition, digital alloy consisting of  $(0.4 \text{ nm}/0.4 \text{ nm}) \times 100 \text{ Al}_{0.52}\text{Ga}_{0.48}\text{As}/\text{AlAs}$  was also used as a sacrificial layer, which shows selectivity towards  $\text{Al}_{0.75}\text{Ga}_{0.25}\text{As}$  using  $\text{HF}:\text{H}_2\text{O} (1:10)$  [44].

The fabrication step using lithography patterning can be carried out with two different methods, as reported recently using rectangular stripe patterns for a  $\text{In}_x\text{Ga}_{1-x}\text{As}/\text{GaAs}$  system [42]. The first method involves the following steps: SiO<sub>2</sub> deposition, photolithographic patterning, freon reactive ion etching (RIE) to transfer the pattern to the SiO<sub>2</sub> layer and inductive coupled plasma (ICP) etching to transfer the pattern to the epitaxial structure down to the sacrificial  $\text{Al}_x\text{Ga}_{1-x}\text{As}$  layer. In the second method, photolithographic patterning was done directly on the epitaxial structure and wet chemical etching ( $\text{H}_2\text{SO}_4:\text{H}_2\text{O}_2:\text{H}_2\text{O} = 1:8:80$ ) was used to transfer the pattern. Once the patterns were defined and all four sides of the sacrificial layer were exposed, as illustrated in figure 2, a timed etch using  $1:5 \text{ HF}:\text{H}_2\text{O}$  was used to laterally remove  $\text{Al}_x\text{Ga}_{1-x}\text{As}$  and release the bilayer from the substrate for rolling. Both methods work for the feature sizes and structures studied, but the first method is preferred for smaller feature sizes to avoid undercutting the bilayer.

### 2.2. Formation process

**2.2.1. Etching time dependence.** The formation process has been monitored in real time as a function of sacrificial layer etching time [45] for  $\text{In}_x\text{Ga}_{1-x}\text{As}/\text{GaAs}$  tubes that rolled up from one end only. It was found that the roll-up rate was highly nonlinear initially, linear at the intermediate stage and saturated for long etching times. In addition, rolling velocity was found

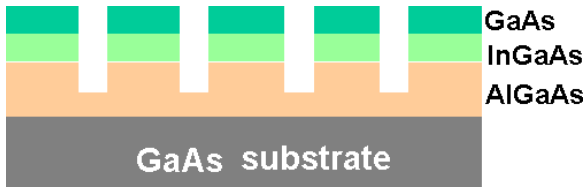


**Figure 2.** Schematic of the cross section of patterned and etched stripe arrays of an InGaAs/GaAs bilayer structure before the AlGaAs sacrificial layer is removed.

to increase with sacrificial layer thickness initially but starts to level off at  $\sim 10$  nm. However, no rolling was observed when the sacrificial layer was thinner than 2 nm. On the other hand, rolling velocity was not affected by tube diameter in the range 20–500 nm. In another report, the formation dynamics of  $\text{In}_{0.2}\text{Ga}_{0.8}\text{As}/\text{GaAs}$  helical structures was demonstrated by releasing a strained bridge by a focused ion beam to form nanoscrolls [29].

Recently we have reported the rolling behaviour at different stages of sacrificial layer undercut using open rectangular mesa geometry [42]. Figure 3 displays a series of SEM images showing the shape evolution of patterned stripes as the tall ( $1.6\ \mu\text{m}$ ) sacrificial layer is removed selectively. When the bilayer begins to be released from the substrate, all four edges start to roll up in the  $[001]$  and  $[010]$  directions (figure 3(a)). As the selective etching proceeds and more of the bilayer is set free, the upward rolling continues for the longer edge, while the shorter edge flattens to allow room for the upward curvature of the longer edge (figure 3(b)). Such geometry dependence enables the formation of single turn mesa by designing the shorter edge (width) of a rectangular mesa to match the tube circumference. Further undercutting leads to the complete rolling of the longer edge and a tube is formed, as shown in figure 3(c). Depending on the width of the released pattern, multi-turn tubes with a high number of rotations can be formed. Shown in figure 4(a) is a multi-turn  $\text{In}_{0.3}\text{Ga}_{0.7}\text{As}/\text{GaAs}$  nanotube rolled from one side of a rectangle while the opposite side is anchored, forming a  $(\text{In}_{0.3}\text{Ga}_{0.7}\text{As}/\text{GaAs})_n$  radial superlattice. Figure 4(b) shows a double multi-turn tube formed by rolling from both directions simultaneously until they are against each other. A theoretical calculation of the radial superlattice of InAs/GaAs predicted real space charge separation across the tube wall thickness [46].

### 2.2.2. Strain direction dependence in SNT formation process.

It can be inferred from the strain induced self-rolling mechanism illustrated in figure 1, that if the strain direction is reversed, e.g. when the compressively strained layer is placed on top of the tensile strained one in the planar structure, the rolling direction should go downwards. This has been observed [42] in a structure where  $\text{In}_{0.2}\text{Ga}_{0.8}\text{As}$  sits on the top and GaAs on the bottom of the bilayer, as shown in figure 5. Multi-turn inverted tubes can also be formed, and the sacrificial layer can be as thin as 10 nm which still allowed the downward rolling of tubes that are 800 nm in diameter, demonstrating the elasticity of those thin walled tubes. Inverted rolling has been demonstrated for other semiconductor tubes made of strained Si [19] or SiGe previously.

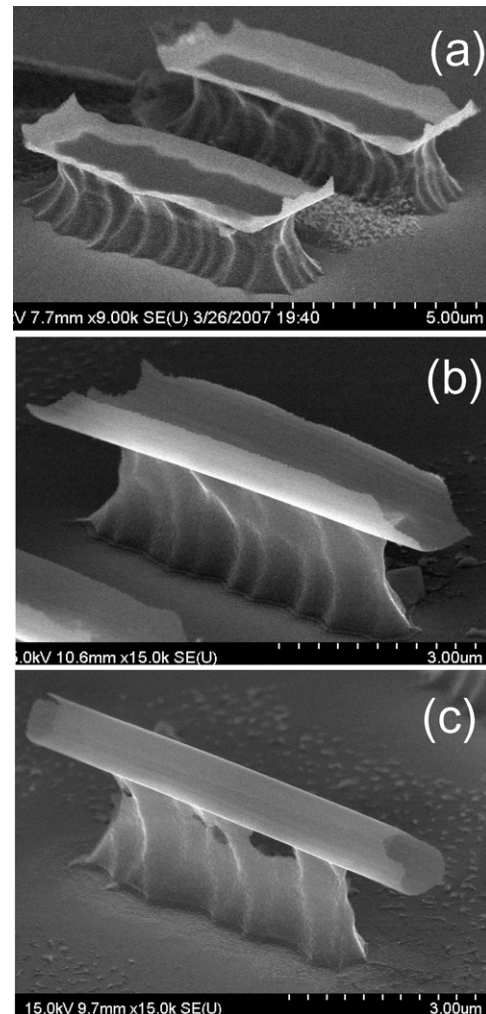


**Figure 3.** SEM images of the nanotube formation process from rectangular stripes: (a) initial stage where all four sides rolling up; (b) as etching proceeds, shorter sides flatten and longer ones continue to roll and (c) the completion of rolling. The longer edge of the rectangle is oriented in the  $[010]$  direction. The tube diameter is measured to be 884 nm. Adapted from [42].

The demonstration of inverted  $\text{In}_x\text{Ga}_{1-x}\text{As}-\text{GaAs}$  tubes is important for tubes with active structures such as quantum wells. In contrast to growing the active structure on top of a strained  $\text{In}_x\text{Ga}_{1-x}\text{As}$  layer, an entire device structure can be grown free of strain before the deposition of the strained rolling-enabling  $\text{In}_x\text{Ga}_{1-x}\text{As}$  layer.

### 2.2.3. Crystal orientation dependence in SNT formation process.

To systematically investigate the crystal orientation dependence of SNT formation, we have used a wheel pattern with eight anchored rectangle stripe pads orientated symmetrically along the  $\langle 100 \rangle$  and  $\langle 110 \rangle$  directions (figure 6(a)). The length of each pad was  $20\ \mu\text{m}$  while the width was  $15\ \mu\text{m}$ , with the foot anchor of  $5\ \mu\text{m}$ .

Shown in figure 6(b) is the result of the  $\text{In}_{0.3}\text{Ga}_{0.7}\text{As}/\text{GaAs}$  bilayer released from the  $(001)$  GaAs substrate using such a wheel pattern [47]. The centre image shows all pads around the wheel while the zoomed in image for each pad is laid out in the outer periphery. It can be seen that the four pads that had the longer edges oriented along the  $\langle 100 \rangle$  directions (diagonal

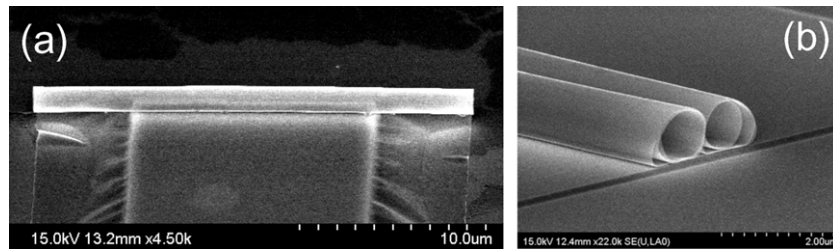


Figure 4. SEM images of multi-turn nanotubes formed by rolling from one side (a) and both sides (b).

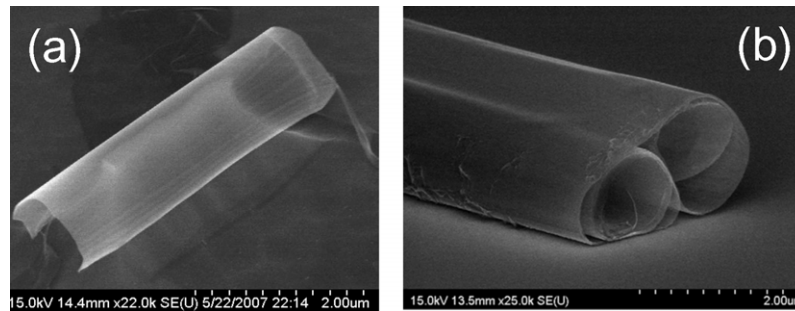


Figure 5. SEM images of inverted rolling of (a) single (partial) and (b) multiple-turn tubes.

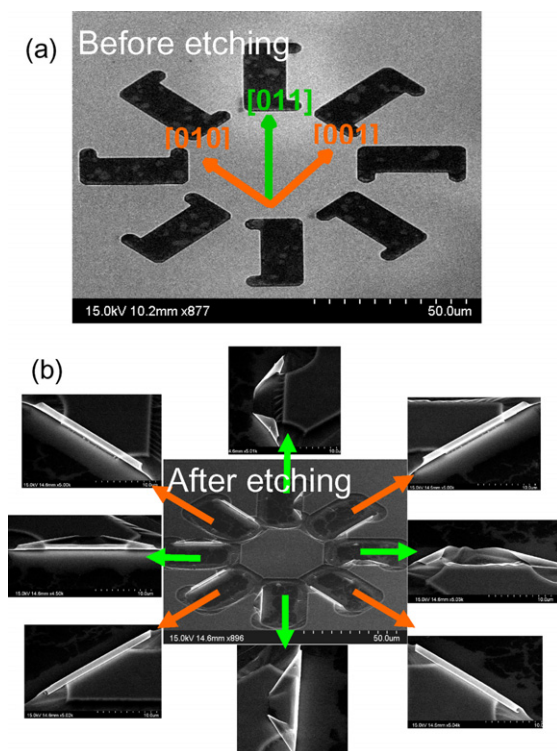


Figure 6. SEM images of the lithographically patterned wheel pattern of anchored rectangular pads (a) before and (b) after etching. The epitaxial film is an  $\text{In}_{0.3}\text{Ga}_{0.7}\text{As}/\text{GaAs}$  film grown on a (100) GaAs substrate. The in-plane crystal orientations are labelled in (a) and colour coded in (b). The high magnification images of all pads after etching are displayed in (b). Adapted from [47].

lines of the wheel, as pointed by orange arrows), formed tubes with rolling took place in the  $\langle 100 \rangle$  direction and stopped at the foot anchors. In contrast, for those four oriented along the  $\langle 110 \rangle$  directions ( $XY$  axes of the wheel, as pointed by

green arrows), the rolling still occurred in the  $\langle 100 \rangle$  directions, which are the corners of the free edges for these pads and thus formed ‘turn-over’ triangular patterns. Continued etching and rolling result in helical structures, as reported in [18, 48, 49].

The persistence of rolling along the  $\langle 100 \rangle$  direction, no matter how the rectangle stripe patterns are oriented, apparently results from the anisotropy of stiffness in cubic GaAs crystals. Cubic crystals show anisotropy in elasticity, photoelasticity and certain other properties not observed in refractive index and conductivity. For GaAs, Young’s modulus in the  $\langle 100 \rangle$  direction is 85.3 GPa, while it is 121.3 GPa in the  $\langle 110 \rangle$  direction [50, 51]. For Si, Young’s moduli along the  $\langle 100 \rangle$  and  $\langle 110 \rangle$  directions are 130.2 GPa and 168.9 GPa, respectively [52]. Theoretical calculations show that the strain energy for the  $\langle 100 \rangle$  winding direction is the smallest [53] for (100) substrates, supporting the crystal dependence observed. For (110) substrates, the preferred rolling direction is  $\langle 110 \rangle$  [54].

In addition to crystal anisotropy in elasticity, chemical etching anisotropy with crystal orientation also impacts the rolling behaviour. Furthermore, sharp edges and corners of the lithographic pattern play a role in rolling details such as right or left hand helix formation [49]. The dependence of the rolling direction on these factors provides the basis for the formation of sophisticated three-dimensional architectures. Shown in figure 7 are arrays of spirals of  $\text{Si}_{0.6}\text{Ge}_{0.4}/\text{Si}/\text{Cr}$  (10/7/20 nm) on Si (100) and (110) substrates [26].

2.2.4. Diameter for strain induced SNTs. Based on the formation mechanism, the diameter of the rolled up tube should be determined by the built-in strain and the total thickness of the bilayer, and the number of rolls should depend on the extent of undercutting. Tubes with diameters from a few nanometres to several micrometres have been formed.

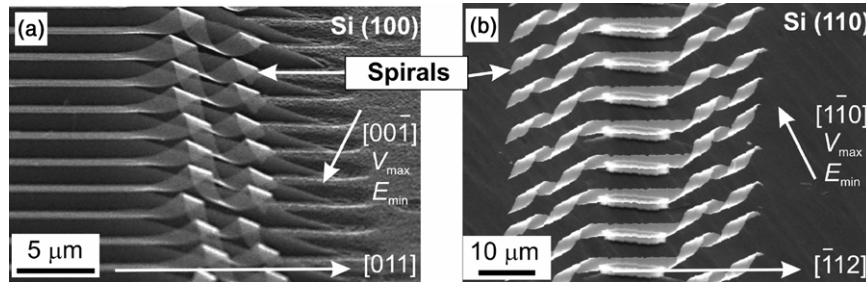


**Figure 7.** SEM images of arrays of spirals of  $\text{Si}_{0.6}\text{Ge}_{0.4}/\text{Si}/\text{Cr}$  (10/7/20 nm) on (a) Si (100) and (b) (110) substrates. Reprinted from [26] copyright 2006 with kind permission of Springer Science and Business Media.

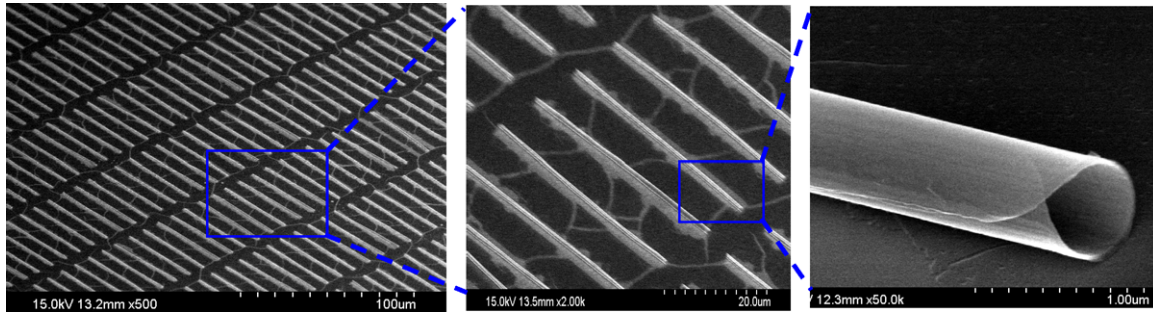


**Figure 8.** Ensemble of  $\text{In}_{0.3}\text{Ga}_{0.7}\text{As}/\text{GaAs}$  nanotubes that are 50  $\mu\text{m}$  in length and 600 nm in diameter, grown by MOCVD epitaxy and fabricated by lithographic patterning and selective etching. Zoomed in images are shown to the right.

The diameter  $D$  for a tubular structure can be calculated using the following equation [55, 56] based on a macroscopic continuous mechanical model:

$$D = \frac{d[3(1+m)^2 + (1+m \cdot n)[m^2 + (m \cdot n)^{-1}]]}{3\varepsilon(1+m)^2},$$

where  $d$  is the total thickness ( $d_1 + d_2$ ),  $m$  is the thickness ratio ( $d_1/d_2$ ),  $n$  is Young's modulus ( $Y_1/Y_2$ ) ratio and  $\varepsilon$  is the lattice mismatch ( $(a_2 - a_1)/a_1$ ) between the two layers.

Although surprising considering the nanoscopic thickness of the films, this macroscopic model has found excellent agreement with the experimentally measured radius, and in most cases the experimental data are smaller than the theoretical value [37, 42, 49, 55]. More sophisticated continuum strain models were evaluated. However, the inclusion of nonlinear strain did not lead to a significant difference, even though the inclusion of anharmonic strain (third order elastic coefficients) led to smaller scroll diameters [53]. The small discrepancy between theory and experiment data in most cases can be corrected by reasonable assumptions of thickness deviation or additional strain. In [22, 57, 58], the authors systematically varied the thickness of the bilayers in two structures,  $\text{In}_{0.33}\text{Ga}_{0.67}\text{As}/\text{GaAs}$  and  $\text{InAs}/\text{GaAs}$ . Experimental data were fitted well using this simple model, when the GaAs layer thickness was corrected with assumed consumption from oxide layer formation. In [25] where the radii of  $\text{Cr}/\text{In}_{0.3}\text{Ga}_{0.7}\text{As}$  tubes were evaluated as a function of Cr layer thickness, the measured radii correspond to an additional internal strain of 0.006 for the Cr layer in order to fit the theoretical curve.

We have varied the composition in the  $\text{In}_x\text{Ga}_{1-x}\text{As}/\text{GaAs}$  bilayer structure from  $x = 0.2$  to 0.3. The thickness has

been verified by scanning transmission electron microscopy and composition by energy dispersion spectroscopy (EDS). The diameters obtained from the rolled up tubes from open ended rectangular mesas are smaller than the theoretical values by 14% [42, 47], corresponding to an additional strain of 0.003. Surface effects, including tension and possible surface reconstruction, have been proposed to be the source of additional strain [59, 60]. In fact, according to Zang *et al*, ultra-thin nanofilms self bend without any external stress load, under internal surface stress imbalance arising from surface reconstruction [60].

### 2.3. Large area assembly of ordered SNT arrays and dispersion of freestanding SNTs on foreign substrates

Controlled positioning of nanotechnology building blocks has always been a challenge, especially with the bottom-up growth method such as for CNTs. Due to the top-down fabrication aspect for strain induced SNTs, it is possible to achieve precise spatial placement of SNTs. Arrays of SiGe bilayer squares ( $30 \times 30 \mu\text{m}^2$ ) rolled up in the diagonal directions have been demonstrated [43], even though the formed microscrolls showed orientation variations that are  $90^\circ$  apart due to the square geometry [42, 43]. High aspect ratio tubes as long as 2 mm have been realized in arrays using a strained 4 nm  $\text{Ga}_{0.3}\text{In}_{0.7}\text{P}/4.4 \text{ nm } \text{Ga}_{0.7}\text{In}_{0.3}\text{P}$  bilayer [22].

We have successfully demonstrated the fabrication of large areas of ordered arrays of  $\text{In}_{0.3}\text{Ga}_{0.7}\text{As}/\text{GaAs}$  SNTs, as shown in figure 8, using lithographically patterned rectangular mesa structures [47, 61]. The tubes are 50  $\mu\text{m}$  in length and  $\sim 590$  nm in diameter, with an aspect ratio of  $\sim 85$ . They are well aligned according to the lithographic design, where the nanotube rolling direction, position, density and aspect ratio

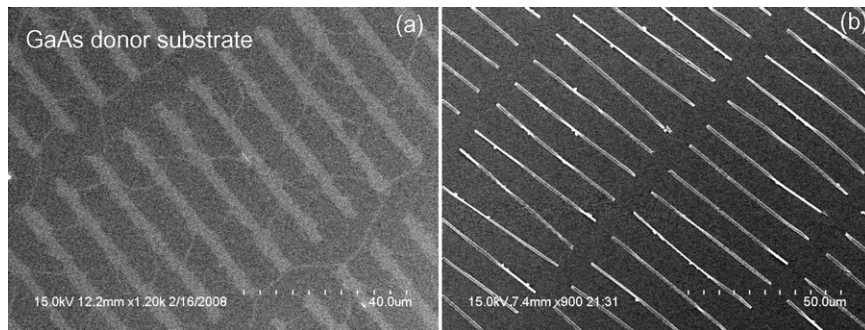


**Figure 9.** SEM images of (a) GaAs donor substrate after the SNT array has been transferred, showing the bare substrate. The colour contrast is due to the height difference as a result of the etching process. (b) In<sub>0.2</sub>Ga<sub>0.8</sub>As/GaAs SNT array on PDMS transferred from the GaAs substrate.

can be readily controlled. Furthermore, the ordered SNT array formation can be scaled to whole wafers, since the processing method used is compatible with existing micro-electronic processing technology. A small degree of inhomogeneity in tube diameter along and between tubes in such arrays has been observed [22, 47]. The precision in lithography patterning alignment can affect the diameter distribution. Etching rate variation across the area is also a possible contributor [43]. Both of these factors can be optimized experimentally.

It is worth noting that the SNTs shown in figure 8 are completely released from the substrate where no chemical bond exists between the substrate and the tubes. The SNTs are tethered on the substrate simply by van der Waals force through surface tension. This allows the release of SNTs from the substrate, their dispersion into solution and subsequent deposition onto a foreign substrate of choice. We have indeed been able to successfully remove In<sub>x</sub>Ga<sub>1-x</sub>As/GaAs SNTs from the GaAs surface where the growth and fabrication took place, and disperse them in methanol by sonication, then deposit them on a silicon substrate [47]. Note that these are hollow tubes with wall thicknesses of ~10–12 nm and diameters on the order of 500–1000 nm. Such dispersion and transfer processes did not seem to damage the structural integrity of the tubes significantly, indicating the mechanical flexibility of the nanoscopic form of materials.

Furthermore, the SNT arrays can be released controllably by high fidelity transfer printing without altering the spatial alignment using the technology developed by Rogers' group [62]. Figure 9 shows the preliminary transfer result by Chun *et al* (to be published) of In<sub>0.2</sub>Ga<sub>0.8</sub>As/GaAs SNT arrays from GaAs substrates to a poly-dimethyl siloxane (PDMS) stamp. It can be seen from figure 9(a) that the SNTs have been completely removed from the native GaAs substrate where the colour contrast indicates GaAs height difference between the stripes (lighter colour) where the SNTs were located and the trenches (darker colour) where undercutting etching took place. The alignment and integrity of the SNTs have mostly been maintained (figure 9(b)) after transfer and work is in progress to improve the fidelity and yield of transfer printing of such 3D high aspect ratio nanoscale structures. This capability opens up the prospect of using SNTs as building blocks on various substrates including applications in flexible nanoelectronics and nanophotonics. The detailed transfer process will be reported separately.

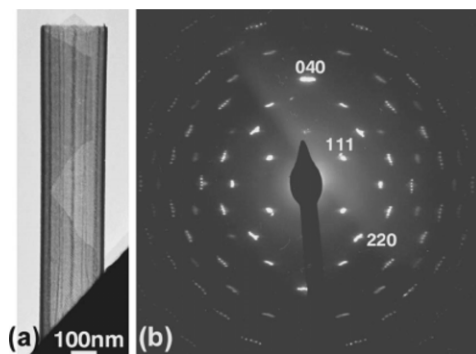


**Figure 10.** (a) Bright field image of an InAs/GaAs SNT with two and one-half turn rotations (b) Selected area electron diffraction (SAED) pattern taken from a region across the entire diameter of the tube and indexed for the reflections of GaAs. Reproduced from [17] copyright 2004 with permission from American Institute of Physics.

### 3. Properties of SNTs and potential applications

SNTs are interesting by themselves due to novel properties induced by the additional degree of freedom—curvature in a semiconductor thin film. The versatile heterojunctions that can be embedded in the tube wall further distinguishes them from other objects with cylindrical symmetry.

In this section, we review the structural, electrical and optical properties of these SNTs characterized by various techniques. We also discuss the potential applications and challenges that must be overcome in order to achieve working devices.

#### 3.1. Structural properties by transmission electron microscopy (TEM) and micro-x-ray diffraction

Shown in figures 10(a) and (b) are a high resolution TEM image from an InAs/GaAs tube and a selective area diffraction pattern taken from across the entire tube diameter, respectively [17, 23, 63]. The clear diffraction pattern indicates high crystal quality of the rolled up layers. All reflections of the lattice planes are elongated into circle segments of diffraction rings, consistent with the nearly perfect cylindrical symmetry. However, the zinc blend four fold symmetry does not appear to be affected by the rolling action [17, 23, 63]. Stacking faults were found in some nanotubes where the rolling involves a misorientation [40].

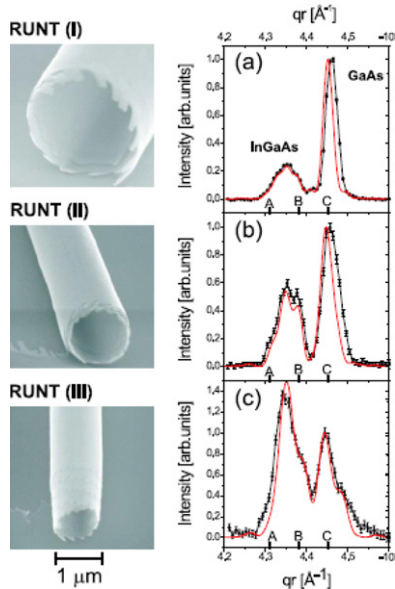


**Figure 11.** X-ray micro-beam diffraction curves for  $\text{In}_x\text{Ga}_{1-x}\text{As}/\text{GaAs}$  individual microtubes from the (004) diffraction. The experimental data are shown in black and simulation is shown in red/grey. See text for explanations. Reproduced from [64] copyright 2006 with permission from American Physical Society. (Colour online.)

TEM has also been done on  $\text{In}_x\text{Ga}_{1-x}\text{As}/\text{GaAs}$  tubes functionalized with a self-assembled monolayer (SAM) of 1-hexadecanethiol, which created a multiperiod inorganic/organic radial superlattice when rolled up with multiple turns [23]. The SAM layer turned out to be stable during the HF underetching process. HR-TEM confirmed the existence of alternating crystalline and non-crystalline layers. Furthermore, the non-crystalline part is shown to be pure hydrocarbon without any amorphous oxide, and no crystalline materials were consumed during the formation of the rolled up superlattice interfaces. This is in contrast to the multiwalled tubes without the organic SAM layers, where non-crystalline amorphous oxide was found [17, 63].

An x-ray micro-diffraction study of individual SNTs on substrates has been reported by Krause *et al* in 2006 [64]. Using the focused x-ray beam with a spot size of  $6 \times 6 \mu\text{m}^2$  and an intensity of  $1 \times 10^9 \text{ photons s}^{-1}$  at an energy of 10 keV from a synchrotron radiation facility, this team was able to probe individual SNTs by limiting the scattering volume to an individual tube. A combination of optical alignment and diffraction was used to locate the tube. For measurements done on  $\text{In}_x\text{Ga}_{1-x}\text{As}/\text{GaAs}$  multiwalled tubes with various diameters, two well-separated Bragg peaks were observed, as shown in figure 11. One peak is close to the bulk GaAs position marked C and one is located between the fully strained  $\text{In}_x\text{Ga}_{1-x}\text{As}$  position A (found in as-grown film perpendicular to the substrate) and the completely relaxed position B (i.e. the  $\text{In}_x\text{Ga}_{1-x}\text{As}$  lattice parameter expected from Vegard's law).

The observation of the two peaks confirms that the crystallinity of the bilayer is maintained in the SNTs. The intermediate position of the  $\text{In}_x\text{Ga}_{1-x}\text{As}$  peak indicates that the rolled up InGaAs layer is only partially relaxed because of the

torsional momentum within the bilayer. For the three different size tubes studied, varied by changing GaAs thickness, the intensity of the partially relaxed  $\text{In}_x\text{Ga}_{1-x}\text{As}$  peak increases as the tube diameter decreases relative to the GaAs peak. In addition, the  $\text{In}_x\text{Ga}_{1-x}\text{As}$  peak seems to be moving towards more relaxation as the tube becomes smaller. Since the smallest tube studied had a diameter of  $\sim 0.5 \mu\text{m}$ , it is not clear how much relaxation a much smaller (e.g.  $< 100 \text{ nm}$ ) tube would approach. The differences in the strain distribution of the subsequent turns were not considered in this paper. However, there seems to be a component in the  $\text{In}_x\text{Ga}_{1-x}\text{As}$  peak that overlaps with the fully relaxed peak (B), which is well resolved in figure 11(b) and appears as a shoulder in figure 11(c).

### 3.2. Thermal properties by Raman scattering

Micro-Raman spectroscopy has been used to characterize vibration mode shifts, broadening as well as appearance of forbidden peaks for individual SNTs. In [17], a freestanding rolled up tube consisting of 14 ML of GaAs and 1.4 ML of InAs was studied. Compared with the Raman spectrum of a GaAs substrate at room temperature, transversal optical (TO) phonon of GaAs was observed, indicating the breaking of selection rules for the (001) surface due to the bending of the bilayer. As for the longitudinal optical (LO) phonon peak, it was found to be broadened asymmetrically and softened by  $4\text{--}6 \text{ cm}^{-1}$  at room temperature. The asymmetry was attributed to the nanometre thickness and possible disordered parts, while the large shift could only be explained by heating of the nanotube (strain induced shift was estimated to be only  $\sim 1.5 \text{ cm}^{-1}$ ). A further shift was induced by increasing the pump laser power. In contrast, the LO phonon peak from the bulk GaAs substrate remained at the same position in the same pumping power range (figure 12). The estimated temperature based on the LO phonon peak shift was as much as  $550 \text{ }^\circ\text{C}$  for a pump power of 1.2 mW and a  $1 \mu\text{m}$  spot size [17]. As a result, after prolonged local heating by the laser beam, the Raman spectrum from the heated tube region showed a peak corresponding to the formation of crystalline  $\beta\text{-Ga}_2\text{O}_3$ . This experiment suggests a significant difference in thermal conductivity within the SNTs compared with bulk material. More studies of the thermal transport properties as a function of the SNT diameter and length would be useful for practical applications.

### 3.3. Electronic transport properties

Non-planar two dimensional electron gas (2DEG) systems have been of interest due to the change in physics with the additional degree of freedom from curvature. SNTs with 2DEG layers incorporated in the wall provide an evenly curved platform for studying the 2D transport properties on cylindrical surfaces.

Experimentally, a big challenge for making transport measurements of rolled up suspended 2DEG systems is to achieve ohmic contacts. Mendach *et al* developed a special lithography contact geometry procedure [48, 65] to form a contacted curved lamella, where metal contacts and leads were predefined before rolling up. The material system studied was a rolled up  $\text{Al}_{0.33}\text{Ga}_{0.67}\text{As}/\text{GaAs}/\text{Al}_{0.33}\text{Ga}_{0.67}\text{As}$  quantum well

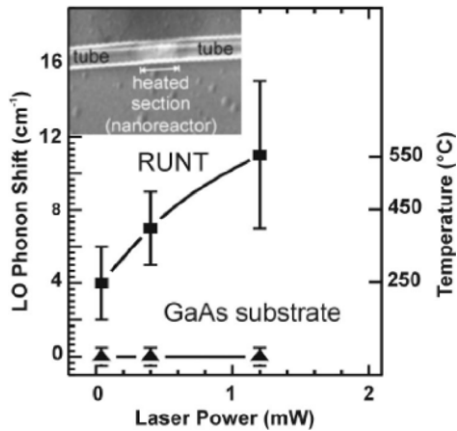


**Figure 12.** LO phonon shift (left axis) and the estimated local temperature (right axis) as a function of laser pump power, obtained from an InAs/GaAs microtube lying on a GaAs substrate (upper left inset). Results taken from the GaAs substrate under the same conditions are shown for comparison. See text for explanation. After [17] copyright 2004 with permission from American Institute of Physics.

structure with Si-delta doping embedded in the  $\text{Al}_{0.33}\text{Ga}_{0.67}\text{As}$  barriers on both sides. Magnetotransport measurements at 4.2 K demonstrated the presence of a curved 2DEG in the lamellas with a magnetoresistance behaviour. Shaji *et al* [66] at the University of Wisconsin–Madison further investigated the topography induced change in magnetoresistance of the electronic system at 2 K. It was found that zero-field resistance increased after the tube formation, which was attributed to an increase in electron scattering along the curved regions due to dangling bonds in the InGaAs layer. At low magnetic fields there existed a negative magnetoresistance, implying the suppression of the curvature induced increase of resistance. However, at high magnetic fields, the resistance started to increase back up almost linearly as a function of the magnetic field. The authors discussed possible electron scattering mechanisms responsible for the different electron transport properties between the tube geometry and its planar counterpart.

In addition to the experimental work, a simulation of high field magnetotransport on a non-planar 2DEG configured in a SNT has been carried out by Meyer *et al* at the University of Wisconsin–Madison [67]. The authors adapted a transfer matrix technique to apply at high magnetic fields to accommodate the non-zero local curvature of the simulated cylindrical resonant quantum cavity system. Conductance in non-planar structures is found to be highly sensitive to the changes in curvature in a wide range of magnetic fields.

The studies so far have elucidated that these systems can be used for probing geometric confinement potentials and achieving topographical quantum systems for potential applications in NEMS and sensing. There is certainly more to be done on the electronic transport properties of the rolled up semiconductor structures both experimentally and theoretically, especially at noncryogenic temperatures.

### 3.4. Optical properties and device prospect

**3.4.1. Optical emission from microtubes with internal light source.** The optical studies of SNTs are mostly done using

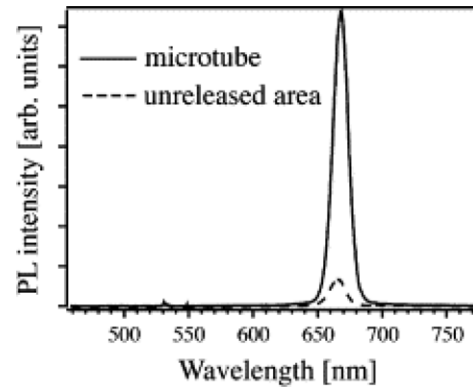


**Figure 13.** Micro-PL spectroscopy at 77 K from the rolled up microtube and its planar counterpart (unreleased area). Reproduced from [68] copyright 2004 with permission from Elsevier.

micro-photoluminescence (PL) spectroscopy on samples that have active light emitting structures, e.g. quantum wells, or quantum dots, incorporated in the tube wall. In all reported cases, optical emission efficiency was enhanced after the structure had been rolled up, which has been attributed to uniaxial-strain effect in the rolled geometry.

Hosoda *et al* [44, 68] fabricated a free standing QW microtube (6–8  $\mu\text{m}$  in diameter) with a 7 nm  $\text{In}_{0.19}\text{Ga}_{0.81}\text{As}$  layer as the wrapper (outer shell of the tube). The QW was 5–7 ML ( $\leq 2$  nm) GaAs with symmetric 10 nm  $\text{Al}_{0.75}\text{Ga}_{0.25}\text{As}$  barrier layers on each side. Although the wall thickness was only 40 nm, PL from the  $\Gamma_1\text{-hh1}$  subband was clearly observed at 77 K. Remarkably, the PL intensity from the QW microtube was much stronger, compared with the before rolling (unreleased) region, as shown in figure 13. The enhanced PL efficiency was attributed to a type II to type I transition as a result of the uniaxial tensile strain the QW experienced after rolling up. The PL peak from the tube showed a slight red shift ( $-31$  meV), which agreed reasonably well with the calculated energy shift of  $\sim -21$  meV, considering the irregularity of tube shape and fluctuation of the inner strain during sample fabrication.

In fact, the strain in a rolled up QW layer depends on its position in the structure due to the balance of force between the top layers and the extended  $\text{In}_x\text{Ga}_{1-x}\text{As}$  wrapper layer [28, 69]. If the QW is near the  $\text{In}_x\text{Ga}_{1-x}\text{As}$  wrapper layer, the strain is tensile; however, when the GaAs QW moves away from the  $\text{In}_x\text{Ga}_{1-x}\text{As}$  layer towards the surface, the strain experiences a neutral plane (zero in strain) and then becomes compressive. A 3 nm GaAs QW positioned in the tensile strain zone is illustrated in figure 14(a) as an example. Shown in figure 14(b) are the calculated and measured peak shifts by cathodoluminescence (CL) at 10 K, caused by internal strain for a 3 nm GaAs QW wrapped in an  $\text{In}_{0.37}\text{Ga}_{0.63}\text{As}$  shell. It clearly shows that the peak shift relative to planar QW of the same structure is changed from red shift to blue shift as the QW is moved away from the  $\text{In}_x\text{Ga}_{1-x}\text{As}$  wrapping layer towards the surface.

In addition to QWs, self-assembled InAs quantum dots were incorporated into  $\sim 10$   $\mu\text{m}$  diameter InGaAs/GaAs tube walls [70]. The QD emission wavelength from the strained layers was slightly red-shifted (10 meV at 7 K) from its

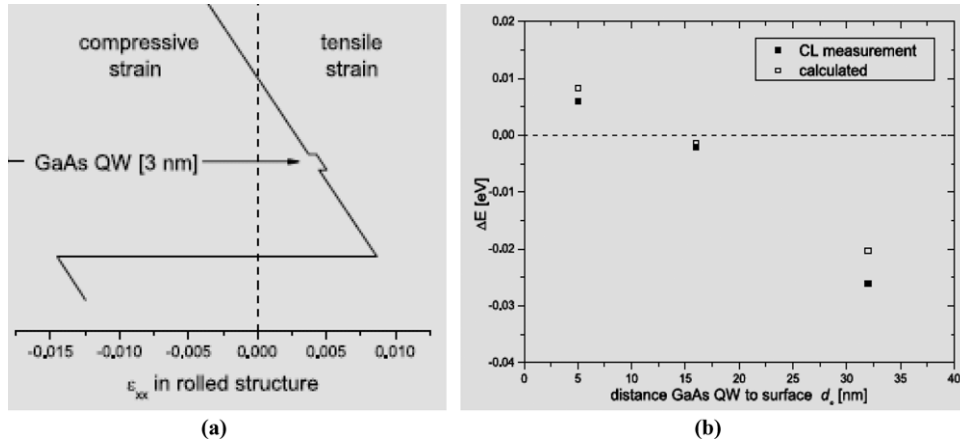


**Figure 14.** (a) Schematic of strain distribution in a rolled up structure with InGaAs as the outer shell (wrapper) and GaAs QW with AlGaAs barriers in the tube walls. Depending on the QW position relative to the InGaAs layer, it could either be tensile or compressive strained. (b) Calculated and measured CL peak shift relative to planar QW, as a function of the GaAs QW distance to the surface. Reproduced from [28] copyright 2006 with permission from Wiley.

planar structure, which was attributed to be a result of strain relaxation, and at the same time the signal intensity increased when rolled up into tubes. This is the same trend observed for QW microtubes described above. Furthermore, light was detected at the tube end, about 50 μm away along the tube axis from the laser excitation spot. This proves the indispensable waveguiding ingredient of optical resonator nature of these tubes, even though the observed wave propagation direction would need to be suppressed in order to achieve whispering gallery mode (total internal reflection) resonators with light circling around (not along) the tube axis. The authors proposed to use narrow rings instead of tubes, i.e. by rolling up thickness modulated layers to confine the waveguiding mode radially.

**3.4.2. Optical resonant modes from semiconductor microtube ring resonators.** Kipp *et al* from the University of Hamburg, Germany, has observed for the first time the optical ring resonant modes in suspended InGaAs/GaAs multi-wall microtubes [71]. Self-assembled InAs quantum dots were embedded in the tube’s wall as the internal emitter and the tube diameter was 5.25 μm. As shown in figure 15, sharp polarized and regularly spaced optical modes were observed from the micro-PL spectrum taken at 5 K, proving the optical ring resonator nature of the microtube. In the supporting analysis, the tube was regarded as a planar dielectric waveguide surrounded by air or other media, or as a dielectric disc with a hole in the centre. At resonance, the propagation of light satisfies the following relationship:  $\pi D \cdot n_{\text{eff}} = \lambda m$ , and  $\Delta\lambda = \lambda^2 / \pi D \cdot n_{\text{eff}}$ , where  $n_{\text{eff}}$  is the effective index of refraction,  $D$  is the tube diameter (cavity length = circumference =  $\pi D$ ) and  $m$  is the azimuthal mode number,  $\lambda$  is the propagating light wavelength. The calculated mode number and corresponding frequency are labelled in figure 18 using both models, which are consistent with experimental data.

As pointed out by the authors [71], the microtube ring resonator potentially has some intrinsic advantages compared with the state-of-the-art microdiscs: (1) InAs QDs exhibit low absorption loss; (2) the microtube surface should be epitaxially smooth in contrast to the dielectric surface of microdiscs, suppressing scattering on surface roughness and (3) most uniquely,

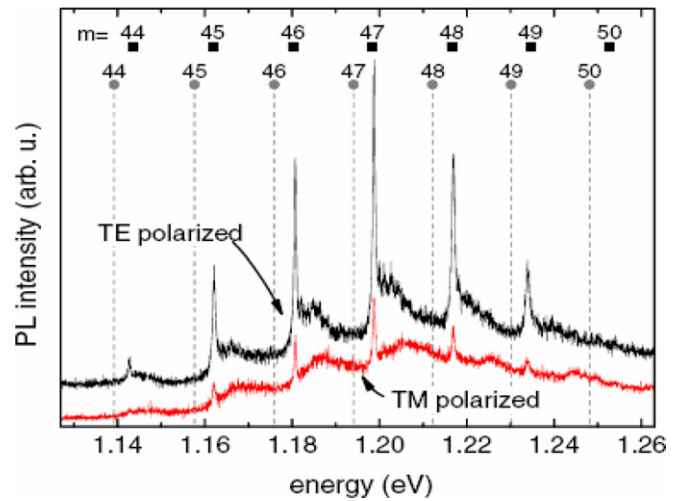


**Figure 15.** Micro-PL spectra at 5 K taken from a suspended InGaAs/GaAs tube with InAs quantum dots incorporated as the internal light source. The azimuthal mode numbers calculated using two different models are labelled, showing reasonable agreement with the experimental data. Reproduced from [71] copyright 2006 with permission from American Physical Society.

the active material is intrinsically located very close to the maximum optical field intensity and there is inherent matching of emitter and optical field in the radial and azimuthal directions.

The unambiguous PL resonance modes have also been observed from Si–SiO<sub>2</sub> rolled up microtubes [72]. The interesting hybrid system of Si–SiO<sub>x</sub> (20 nm partially relaxed–20 nm) nanotubes was examined by micro-PL spectroscopy [72, 73] at room temperature. The authors treated the Si–SiO<sub>x</sub> nanotubes with rapid thermal annealing at 850 °C for 30 min, suggesting the high thermal stability of such tubular structures. The resulting tube presumably contained Si nanoclusters embedded in the SiO<sub>x</sub> amorphous layer. The modulated PL spectrum from the freestanding tube area indicates the presence of optical resonant modes at certain wavelengths of light, through total internal reflection at the curved surface.

In both cases, lasing was not achieved. A quality factor  $Q$  of ~3000 was measured for the InGaAs/GaAs tube, in contrast

to a calculated  $Q$  that was orders of magnitude higher, and that for state-of-the-art micro-cavities used in cavity quantum electrodynamic (CQED) experiments [71]. A complete three-dimensional confinement of light by suppressing wave propagation along the tube axis is needed in order to achieve a higher  $Q$  factor. Further optimization of gains, losses and heat conduction to the substrate is needed. In particular, the loss from the discontinuous radii in the region of the stricture in the tube wall needs to be minimized. A novel interlocking mechanism was recently used to fabricate closed InGaAs/GaAs microtubes with precisely tunable parameters, for potentially low loss optical resonators [74].

Looking beyond the optically pumped resonator, in order to achieve electrically pumped lasing in such resonators, metal contact issues need to be addressed. Metal contacts and isolations are almost always the most difficult part of the fabrication for any electrically injected nanoscale devices, especially for those grown with bottom-up approaches. With the top-down aspect in the fabrication of strain induced III-V semiconductor tubes, metal contact and isolation scheme should be more manageable, owing to the precise spatial placement of the tubes. The well-established contact formation processes in planar III-V semiconductor optoelectronics devices will be a valuable resource. Preliminary ideas and results using a two-step metal evaporation process have been reported [15, 65]. The process involves using the lithographic method to predetermine the location and the length of the forming tubes, which enables the metal layers to roll-in at predefined positions forming contacts. For the electrical operation of rolled up 3D devices, contacts on both the p-side and the n-side are required and need to be addressed individually and integrated with supporting devices.

## 4. Other strain-driven 3D architectures and applications

### 4.1. High precision self-folding MEMS

Typical micro-electrical and mechanical systems (MEMSs) devices include hinged parts that are released from the substrate and fixed in a defined position or remain movable during device operation. Based on the concept of strained induced self-rolling, a method analogous to the Japanese paper folding micro-origami technique, was used to produce arrays of MEMS components [41]. The main idea of the concept, as illustrated in figure 16, is to use multiple strained bilayers sandwiched by sacrificial layers and step by step lithography patterning to sequentially release parts of the structure in desired directions.

Shown in figures 17(a) and 17(b) are images of various MEMS objects formed using this method. As is the case for fully rolled up tubes, curvatures of these MEMS components are determined by the amount of strain and thickness for a specific material. More complex micro-machined structures using this approach are promising for different applications in optical MEMS devices such as mirrors, diffractive lenses and switches, etc.

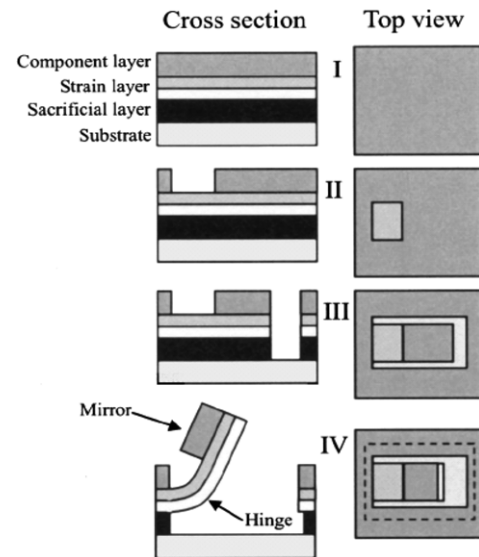


**Figure 16.** Schematic of a four-step fabrication procedure for micro-origami structures. Reproduced from [41] copyright 2003 with permission from American Institute of Physics.

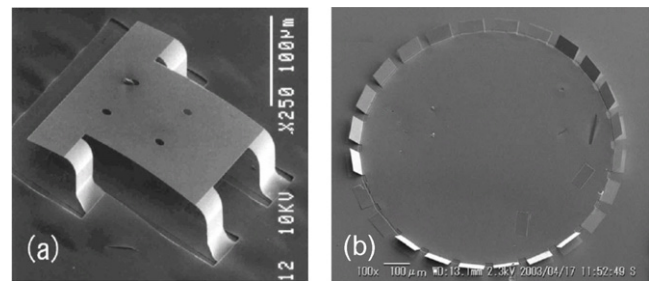


**Figure 17.** (a) SEM image of an  $\text{In}_x\text{Ga}_{1-x}\text{As-GaAs}$  micro-stage with hinge length of  $27\ \mu\text{m}$  using valley and mountain fold methods. Reproduced from [75] copyright 2003 with permission from Elsevier. (b) SEM image of a ring of  $\text{In}_x\text{Ga}_{1-x}\text{As-GaAs}$  micro-mirrors with a  $5.5\ \mu\text{m}$  long hinge for optical actuation. Reproduced from [76] copyright 2003 with permission from American Institute of Physics.

Compared with conventional Si-based MEMS, the III-V based micro-origami method has the advantages of self-positioning precision and versatility. At the same time, it could be strongly influenced by the fabrication process [77]. With the controlled fabrication process, micro-origami method is expected to become a viable fundamental technique for developing MEMS devices with complex three-dimensional structures.

### 4.2. Nanocorrugated quantum structures and wrinkled nanomembranes

The method making it possible to detach strained bilayer films from substrates has also been applied to the case of single and sandwiched strained layers.

In particular, a corrugated film was fabricated consisting of alternating locally bent regions with locally modified electronic states on a nanometre scale. When  $\text{In}_x\text{Ga}_{1-x}\text{As}$  is sandwiched between two sacrificial layers and topped by a cap layer and bottomed by the substrate (figure 18), buckling of the  $\text{In}_x\text{Ga}_{1-x}\text{As}$  layer emerges in a self-formed manner once

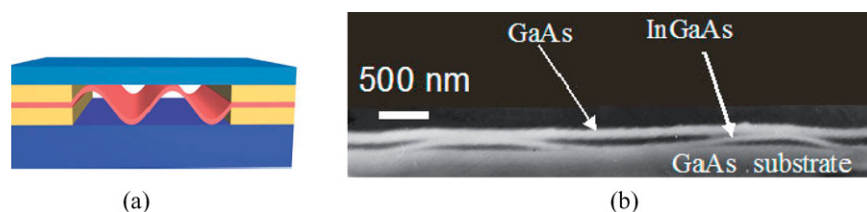


**Figure 18.** (a) Schematic of a nanocorrugated quantum system with periodically buckled layer between the cap layer and the substrate. (b) SEM image of buckled InGaAs layer between GaAs cap and substrate. Reproduced from [79] copyright 2006 with permission from Wiley.

the sacrificial layer is removed [78–80]. The shape of the corrugated structure is close to a sinusoid. The precise corrugation amplitude and period are determined by its lattice mismatch to the substrate, as well as the length of the free standing film and the free space height (distance between cap and substrate). The band structure in each of the bent regions differs from that in a flat film. It was shown theoretically that in InAs films thinner than 4 nm, the elastic strain gives rise to a periodic potential consisting of quantum wells that are a few electronvolts deep [80]. Nanocorrugated films represent new self-assembled periodic quantum systems with geometrical confinement.

Another type of strain-driven structure that is formed upon releasing from the substrate consists of strain-sharing tri-layer nanomembranes, such as GaAs/In<sub>x</sub>Ga<sub>1-x</sub>As/GaAs and Si/Si<sub>1-x</sub>Ge<sub>x</sub>/Si thin films with a typical thickness of each layer less than a few tens of nanometres, as reviewed recently [81]. An interesting phenomenon for such nanomembranes is the periodic wrinkling in various directions that forms nanochannel networks [82]. A recent report on the study of optical properties of wrinkled III–V semiconductor membranes showed similar trends as rolled up SNTs in terms of PL peak shift and intensity in contrast to planar films, and the enhanced light emission has been explained by interference contrast theory [83].

## 5. Conclusions

Strain induced self-rolling semiconductor micro- and nanotubes and related structures represent a new class of building blocks of nanotechnology. Although pioneering work on fabrication and characterization has been performed, this is an emerging field that remains relatively unexplored. In this paper, the formation method, process and dependence on crystal orientation, strain direction as well as geometry have been reviewed, and their implications have been explored. The structural, thermal, electronic and optical properties of these tubes have been summarized. Potential applications and challenges have been discussed.

The author's vision for this exciting new field has two aspects: (1) SNTs as new nanotechnology building blocks for planar devices; (2) SNTs as vehicles for creating 3D active architectures, by incorporating active device structures in the tubular frame. The first aspect requires small diameters and is analogous to the function of other nanotechnology building blocks such as CNTs, quantum dots, quantum wires and quantum wells. The second aspect of the SNT functionality can be regarded as analogous to chemically functionalizing

quantum dots or CNTs; however, the functionalization is not simply carried out by changing the surface properties but rolling up functional device structures into the tube wall.

Compared with other building blocks, strain induced SNTs are advantageous in the following ways: (1) precise positioning due to the top-down aspect of the fabrication approach; (2) versatility in functionality due to the availability of semiconductor materials and the ability to form heterojunctions, hybrid structures with organic and biomaterials, metals, dielectrics and piezoelectrics, etc. (3) uniqueness in geometry for its large surface to volume ratio and flexibility in architecture building. These may lead to breakthroughs in drug delivery, highly sensitive, handheld chemical and biological sensors and next generation nanoelectronic and nanophotonic devices.

## Acknowledgment

This work was supported by the University of Illinois and the National Science Foundation CAREER award ECCS 07-47178. Li would like to acknowledge her students Ik Su Chun, Kevin Bassett and Ryan Dowdy for their contributions, and Professor James J Coleman and John A Rogers for their support.

## References

- [1] Iijima S 1991 *Nature* **354** 56
- [2] Dai H, Rinzler A G, Nikolaev P and Thess A 1996 *Chem. Phys. Lett.* **260** 471
- [3] Meyyappan M, Delzeit L, Cassell A and Hash D 2003 *Plasma Sources Sci. Technol.* **12** 205
- [4] Oncel C and Yurum Y 2006 *Fullerenes Nanotubes Carbon Nanostruct.* **14** 17
- [5] Melechko A V, Merkulov V I, McKnight T E, Guillorn M A, Klein K L, Lowndes D H and Simpson M L 2005 *J. Appl. Phys.* **97** 41301
- [6] Smalley R E, Li Y, Moore V C, Price B K, Colorado R Jr, Schmidt H K, Hauge R H, Barron A R and Tour J M 2006 *J. Am. Chem. Soc.* **128** 15824
- [7] Kingston C T and Simard B 2006 *J. Nanosci. Nanotechnol.* **6** 1225
- [8] Thostenson E T, Zhifeng R and Tsu-Wei C 2001 *Compos. Sci. Technol.* **61** 1899
- [9] Meitl M A, Yangxin Z, Gaur A, Seokwoo J, Usrey M L, Strano M S and Rogers J A 2004 *Nano Lett.* **4** 1643
- [10] Heller D A, Jeng E S, Yeung T-K, Martinez B M, Moll A E, Gastala J B and Strano M S 2006 *Science* **311** 508
- [11] Bandaru P R 2007 *J. Mater. Sci.* **42** 1809
- [12] Delzeit L, Cassell A, Hash D and Meyyappan M 2003 *Plasma Sources Sci. Technol.* **12** 205

- [13] Belin T and Epron F 2005 *Mater. Sci. Eng. B* **119** 105
- [14] Grimes C A, Mor G K, Varghese O K, Paulose M and Shankar K 2006 *Sol. Energy Mater. Sol. Cells* **90** 2011
- [15] Prinz V Y, Seleznev V A, Gutakovskiy A K, Chehovskiy A V, Preobrazhenskii V V, Putyato M A and Gavrilova T A 2000 *Physica E* **6** 828
- [16] Golod S V, Prinz V Y, Mashanov V I and Gutakovskiy A K 2001 *Semicond. Sci. Technol.* **16** 181
- [17] Deneke C, Jin-Phillipp N Y, Loa I and Schmidt O G 2004 *Appl. Phys. Lett.* **84** 4475
- [18] Prinz V Y 2003 *Microelectron. Eng.* **69** 466
- [19] Songmuang R, Deneke C and Schmidt O G 2006 *Appl. Phys. Lett.* **89** 223109
- [20] Nastaushev Y V, Prinz V Y and Svitashva S N 2005 *Nanotechnology* **16** 908
- [21] Luchnikov V and Stamm M 2007 *Physica E* **37** 236
- [22] Schmidt O G, Deneke C, Kiravittaya S, Songmuang R, Heidemeyer H, Nakamura Y, Zapf-Gottwick R, Muller C and Jin-Phillipp N Y 2002 *IEEE J. Sel. Top. Quantum Electron.* **8** 1025
- [23] Deneke C, Zschieschang U, Klauk H and Schmidt O G 2006 *Appl. Phys. Lett.* **89** 263110
- [24] Schmidt O G, Schmarje N, Deneke C, Muller C and Jin-Phillipp N Y 2001 *Adv. Mater.* **13** 756
- [25] Schumacher O, Mendach S, Welsch H, Schramm A, Heyn C and Hansen W 2005 *Appl. Phys. Lett.* **86** 143109
- [26] Prinz V Y and Golod S V 2006 *J. Appl. Mech. Tech. Phys.* **47** 867
- [27] Golod S V, Prinz V Y, Wagli P, Zhang L, Kirfel O, Deckhardt E, Glaus F, David C and Grutzmacher D 2004 *Appl. Phys. Lett.* **84** 3391
- [28] Paetzelt H, Gottschalch V, Bauer J, Herrnberger H and Wagner G 2006 *Phys. Status Solidi a* **203** 817
- [29] Yeoh T, Mason M, Feinberg Z, Leung M, Tasci M, Elarde V C and Coleman J J 2006 *Mater. Res. Soc. Symp. Proc.* **924** Z06
- [30] Zhang L, Deckhardt E, Weber A, Schonenberger C and Grutzmacher D 2005 *Nanotechnology* **16** 655
- [31] Schmidt O G and Eberl K 2001 *Nature* **410** 168
- [32] Prinz A V, Prinz V Y and Seleznev V A 2003 *Microelectron. Eng.* **67–8** 782
- [33] Prinz V Y, Chehovskiy A V and Nenasheva L A 1999 *Nanostructures: Physics and Technology. 7th Int. Symp.* 481
- [34] Schmidt O G, Deneke C, Manz Y M and Muller C 2002 *Physica E* **13** 969
- [35] Deneke C and Schmidt O G 2006 *Appl. Phys. Lett.* **89** 123121
- [36] Thurmer D J, Deneke C, Yongfeng M and Schmidt O G 2006 *Appl. Phys. Lett.* **89** 223507
- [37] Giordano C, Todaro M T, Salhi A, Martiradonna L, Viola I, Passabi A, Carbone L, Gigli G, Passaseo A and De Vittorio M 2007 *Microelectron. Eng.* **84** 1408
- [38] Prinz A V and Prinz V Y 2003 *Surf. Sci.* **532–535** 911
- [39] Seleznev V, Yamaguchi H, Hirayama Y and Prinz V 2003 *Japan. J. Appl. Phys. Part* **42** 791
- [40] Prinz V Y, Chekhovskiy A V, Preobrazhenskii V V, Semyagin B R and Gutakovskiy A K 2002 *Nanotechnology* **13** 231
- [41] Ocampo J M Z, Vaccaro P O, Fleischmann T, Wang T-S, Kubota K, Aida T, Ohnishi T, Sugimura A, Izumoto R, Hosoda M and Nashima S 2003 *Appl. Phys. Lett.* **83** 3647
- [42] Chun I S, Verma V B, Elarde V C, Kim S W, Zuo J M, Coleman J J and Li X 2008 *J. Cryst. Growth* **310** 2353
- [43] Qin H, Shaji N, Merrill N E, Kim H S, Toonen R C, Blick R H, Roberts M M, Savage D E, Lagally M G and Celler G 2005 *New J. Phys.* **7** 1
- [44] Hosoda M, Kishimoto Y, Sato M, Nashima S, Kubota K, Saravanan S, Vaccaro P O, Aida T and Ohtani N 2003 *Appl. Phys. Lett.* **83** 1017
- [45] Deneke C and Schmidt O G 2004 *Appl. Phys. Lett.* **85** 2914
- [46] Osadchii V M and Prinz V Y 2000 *JETP Lett.* **72** 312
- [47] Chun I S and Li X 2008 *IEEE Trans. Nanotechnol.* **7** 493
- [48] Mendach S, Schmacher O, Heyn C, Schnull S, Welsch H and Hansen W 2004 *Physica E* **23** 274
- [49] Zhang L, Golod S V, Deckardt E, Prinz V and Grutzmacher D 2004 *Physica E* **23** 280
- [50] Cottam R I and Saunders G A 1973 *J. Phys. C: Solid State Phys.* **6** 2105
- [51] Brantley W A 1973 *J. Appl. Phys.* **44** 534
- [52] Wortman J J and Evans R A 1965 *J. Appl. Phys.* **36** 153
- [53] Grundmann M 2003 *Appl. Phys. Lett.* **83** 2444
- [54] Paetzelt H, Gottschalch V, Bauer J and Wagner G 2007 *J. Cryst. Growth* **298** 648
- [55] Vaccaro P O, Kubota K and Aida T 2001 *Appl. Phys. Lett.* **78** 2852
- [56] Tsui Y C and Clyne T W 1997 *Thin Solid Films* **306** 52
- [57] Deneke C, Muller C and Schmidt O G 2002 *Mater. Res. Soc. Symp. Proc.* **728** 141
- [58] Deneke C, Muller C, Jin-Phillipp N Y and Schmidt O G 2002 *Semicond. Sci. Technol.* **17** 1278
- [59] Zang J and Liu F 2007 *Nanotechnology* **18** 405501
- [60] Zang J, Huang M and Liu F 2007 *Phys. Rev. Lett.* **98** 146102
- [61] Chun I S, Verma V B and Li X 2008 *Mater. Res. Soc. Symp. Proc.* **1057** 40
- [62] Sun Y, Kim H-S, Menard E, Kim S, Adesida I and Rogers J A 2006 *Small* **2** 1330
- [63] Jin-Phillipp N Y, Thomas J, Kelsch M, Deneke C, Songmuang R and Schmidt O G 2006 *Appl. Phys. Lett.* **88** 033113
- [64] Krause B, Mocuta C, Metzger T H, Deneke C and Schmidt O G 2006 *Phys. Rev. Lett.* **96** 165502
- [65] Mendach S, Schumacher O, Welsch H, Heyn C, Hansen W and Holz M 2006 *Appl. Phys. Lett.* **88** 212113
- [66] Shaji N, Qin H, Blick R H, Klein L J, Deneke C, and Schmidt O G 2007 *Appl. Phys. Lett.* **90** 042101
- [67] Meyer G J and Knezevic I 2007 *J. Comput. Electron.* **6** 219
- [68] Ohtani N, Kishimoto K, Kubota K, Saravanan S, Sato Y, Nashima S, Vaccaro P, Aida T and Hosoda M 2004 *Physica E* **21** 732
- [69] Kubota K, Vaccaro P O, Ohtani N, Hirose Y, Hosoda M and Aida T 2002 *Physica E* **13** 313
- [70] Mendach S, Songmuang R, Kiravittaya S, Rastelli A, Benyoucef M and Schmidt O G 2006 *Appl. Phys. Lett.* **88** 111120
- [71] Kipp T, Welsch H, Strelow C, Heyn C and Heitmann D 2006 *Phys. Rev. Lett.* **96** 077403
- [72] Songmuang R, Rastelli A, Mendach S and Schmidt O G 2007 *Appl. Phys. Lett.* **90** 091905
- [73] Songmuang R, Rastelli A, Mendach S, Deneke C and Schmidt O G 2007 *Microelectron. Eng.* **84** 1427
- [74] Mendach S, Kipp T, Welsch H, Heyn C and Hansen W 2005 *Semicond. Sci. Technol.* **20** 402
- [75] Vaccaro P O, Kubota K, Fleischmann T, Saravanan S and Aida T 2003 *Microelectron. J.* **34** 447
- [76] Zanardi Ocampo J M *et al* 2004 *Microelectron. Eng.* **73–74** 429
- [77] Huang M, Boons C, Roberts M, Savage D E, Lagally M G, Shaji N, Qin H, Blick R, Nairn J A and Liu F 2005 *Adv. Mater.* **17** 2860
- [78] Prinz V Y 2004 *Physica E* **24** 54
- [79] Prinz V Y 2006 *Phys. Status Solidi b* **243** 3333
- [80] Osadchii V M and Prinz V Y 2005 *Phys. Rev. B* **72** 33313
- [81] Scott S A and Lagally M G 2007 *J. Phys. D: Appl. Phys.* **40** R75
- [82] Mei Y F, Thurmer D J, Cavallo F, Kiravittaya S and Schmidt O G 2007 *Adv. Mater.* **19** 2124
- [83] Mei Y F, Kiravittaya S, Benyoucef M, Thurmer D J, Zander T, Deneke C, Cavallo F, Rastelli A and Schmidt O G 2007 *Nano Lett.* **7** 1676